AIAA JOURNAL
Vol. 31, No. 3, March 1993

Fluorescence Imaging of OH and NO in a Model Supersonic Combustor

Mark G. Allen,[*] Terence E. Parker,[*] William G. Reinecke,[*] Hartmut H. Legner,[*] Richard R. Foutter,[†]
W. Terry Rawlins,[‡] and Steven J. Davis[*]
Physical Sciences, Inc., Andover, Massachusetts 01810

Recent results are presented from an experimental study to develop Planar Laser-Induced Fluorescence (PLIF) diagnostics for application to scramjet combustor development. The measurements are made in a reacting flow shock-tunnel facility which generates Mach 3 air at static conditions of 1500 K and 0.3 atm. Hydrogen or other gases may be injected into the rectangular test section downstream of a rear-facing step. PLIF measurements of NO, naturally present in the reflected shock-heated, freestream air, are used to determine basic flow features, and a technique is demonstrated for determining static temperature variations in nonreacting, nonmixing portions of the flow. PLIF measurements of OH are used to reveal the instantaneous reaction zone interface from a dual round jet injector configuration. Issues associated with quantitative PLIF data interpretation in compressible reacting flows are discussed in detail.

I. Introduction

RENEWED interest in supersonic/hypersonic cruise vehicle development has resulted in increased experimental and computational activity in the area of turbulent, compressible, reacting flows. Progress in nonintrusive optical diagnostic techniques now permit a more thorough understanding of the reacting flow path than can be inferred from wall measurements alone. A particularly useful technique for time-resolved, multidimensional measurements of a variety of in-stream flow parameters in Planar Laser-Induced Fluorescence (PLIF). Recently, several examples of PLIF measurements in supersonic/hypersonic reacting flows have appeared.[1-4] This article discussed details of an experimental program to develop approaches for quantitative measurements of OH and NO distributions in a scramjet combustor simulation test facility. As will be discussed below, the NO distributions can be used to measure the temperature distribution in nonreacting, nonmixing regions of the flowfield.

A. Experimental Facility

The experiments described in this article were performed in a shock tunnel configured to operate at Mach 3.0 with a two-dimensional half-nozzle expanding to a 7.62-cm square cross section. This is followed by a 1.27-cm rearward facing step in one of the four walls. Hydrogen injection ports (diameter = 0.48 cm) are included in the tunnel wall after the rearward facing step along the tunnel centerline at 2.3 and 8.4 step heights downstream, and are directed at 30- and 60-deg angles with respect to the tunnel flow. The shock tube used to drive the shock tunnel is a 15.6-cm-diam system consisting of a 4-m driver section, a 14-m shock tube, a transition section/secondary diaphragm station for separating the shock tube from the tunnel flow section, and a dump tank after the tunnel flow section. The relationship between test time and flow temperatures is between 1 and 3 ms for stagnation temperatures between 4000 and 2500 K, respectively. Static flow pressures for the reported tests are approximately 0.5 atm, but are not limited to this value.

The tunnel test section, beginning at the exit of the Mach 3 half-nozzle, is 2.4-m in length. Wall-mounted pressure taps located along the nozzle and the top of the tunnel test section are used to verify proper performance during a run. Optical access is provided at several locations in the tunnel. The first is immediately after the full expansion point for the nozzle and includes three 4.45-cm clear aperture fused-silica windows. Immediately downstream of the rear-facing step are two full-height windows providing full optical access for the first 14 cm of the flowfield. Smaller windows on the top of the tunnel provide laser access for the PLIF measurements. A schematic of the test section showing the optical access is shown in Fig. 1.

Figure 2 illustrates the expected flow over the rearward facing step without injection. The interaction of the supersonic flow with the step creates an expansion fan that begins at the step corner with a leading edge oriented with a 19.5-deg angle ($\sin^{-1} 1/M$) to the flow. The expansion fan extends from this beginning ray to a recirculation region starting 23-deg below the horizontal. On the other edge of the uniform flow region is a recirculation zone whose extent can be estimated from previous results.[5-8] A recompression shock is introduced by the wall and turns the flow so that it proceeds directly down the duct.

The flowfield after the rearward facing step with injection is more complex and a detailed estimate of the features of this flow is beyond the scope of this article. Figure 3 illustrates

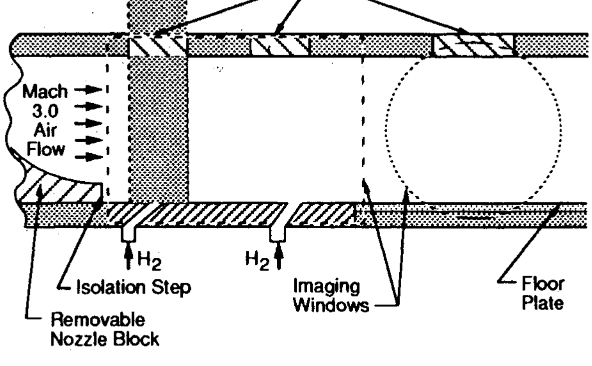

Fig. 1 Shock-tunnel test section schematic.

Received Oct. 18, 1991; revision received July 16, 1992; accepted for publication Aug. 11, 1992. Copyright © 1992 by the American Institute of Aeronautics and Astronautics, Inc. All rights reserved.

[*] Principal Research Scientist, 20 New England Business Center. Member AIAA.

[†] Senior Scientist, 20 New England Business Center. Member AIAA.

[‡] Principal Research Scientist, 20 New England Business Center.

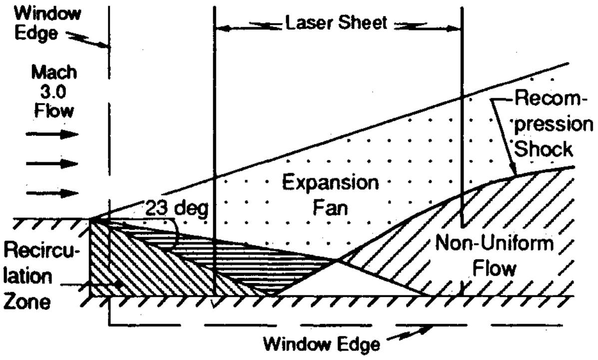

Fig. 2 Graphic representation of the flowfield in the shock tunnel without injection.

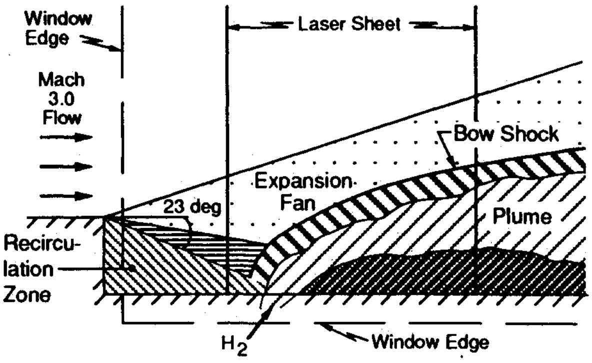

Fig. 3 Graphic representation of the flowfield in the shock tunnel with injection along the centerline of the tunnel.

the gross flow features along the central axial plane. The injectant plume produces a bow shock in a similar fashion to that produced by a solid body in supersonic flow. Following this shock is the plume itself and a thin mixing region where the injectant and freestream air meet. The plume, initially oriented at a 30-deg angle to the flow, spreads as it proceeds downstream and gradually aligns itself with the flow.

B. PLIF Measurement System

The fluorescence experiments in this program were accomplished using an excimer-pumped dye laser system. The dye laser permits continuous wavelength generation from ~320 to over 1000 nm. With the addition of BBO (β-barium borate) doubling crystals, the UV coverage was extended to below 220 nm. The imaging detector system developed for these measurements consisted of a high-resolution, intensified, CCD array photodetector with custom-designed control electronics, interfaced to a personal computer using a commercially available frame grabber. For synchronization with the tunnel flow, both the laser and the intensified camera system were triggered using a signal from the first pressure transducer in the shock tube. The PLIF measurement time could be adjusted with internal delays to occur anytime during the tunnel test time.

Fluorescence originating from the laser-excited plane in the flowfield was collected by a Nikon f = 105 mm, F/4.5 UV-Nikkor lens and focused through sets of Schott glass filters (depending on the particular experiment) onto the camera. The filters eliminated elastic scattering of the laser sheet from windows and walls within the tunnel. Raw PLIF images are corrected for the integrated dark current during the exposure period, spatial variations in the responsivity of the detector array, and nonuniformities in the laser excitation sheet in order to yield the true fluorescence distribution.

II. LIF Measurement Strategies for NO and OH

Acquisition of meaningful fluorescence images in any environment requires a carefully developed strategy for laser excitation and data interpretation. In this section, we present the details of the strategies developed in this program for quantitative OH and NO PLIF measurements. In contrast to the bulk of PLIF diagnostic development, which has been carried out in isobaric, atmospheric pressure flames and flows, the diagnostic strategies developed in this program are tailored to yield meaningful information over a broad range of temperatures (250–3000 K), pressures (0.1–2 atm), and directed velocities (0–200,000 cm/s). Any given PLIF image may traverse regions of widely varying properties. In order to interpret the resulting fluorescence distribution, we must consider variable absorption line widths, velocity-dependent Doppler-shifts of the absorbing line shape, and pressure-, temperature-, and composition-dependent energy transfer within the probed molecule. As we will show, careful selection of the excitation and detection strategy can adjust the measurement sensitivity to these varying parameters.

NO is a particularly important species for these types of flows due to its relatively high concentration in the reflected shock-heated freestream air. This provides an essentially constant mole-fraction constituent of the airflow (in the absence of fuel injection) and allows interrogation of temperature (and ultimately, velocity) fields. In the current experiments, 1–3% NO is present in the freestream air. We have used it primarily as a measure of the base flow characteristics without injection in both the qualitative (i.e., position and angle of key shocks) as well as quantitative (temperature distributions) sense. The OH radical is a key intermediate in hydrocarbon and hydrogen combustion. In the near injector region, it indicates the position of the stoichiometric fuel/air interface where reactions are occurring. Further downstream, the OH radical is a stable, equilibrium species in the high temperature combustion product gases, and can be used to infer the extent of the fuel burning and spreading.

In general, we can express the fuorescence signal viewed by each pixel on the detector array as

$$S_F = (I_\nu B) \cdot (F_y) \cdot (f_B N_t V_c) \cdot (\eta \Omega / 4\pi) \cdot \tau_p \tag{1}$$

where

I_ν = laser spectral intensity
B = Einstein B coefficient for absorption
F_y = fluorescence yield
f_B = Boltzmann population fraction
N_t = species number density
V_c = collection volume
η = filter transmission, detector responsivity, etc.
Ω = collection solid angle of imaging system
τ_p = pulse duration

The first parenthetical term is the probability per unit time that laser absorption will occur. It depends on the local laser energy (which, in general, varies across the laser sheet) and the Einstein B-coefficient (which is constant for a selected transition). The second parenthetical term is the probability that an absorption event will result in a fluorescence photon. In general, it is the ratio of the radiative decay rate over all possible decay rates from the laser excited state. The exact form of the expression for the fluorescence yield, therefore, depends on the particular strategies employed for a given molecule and will be discussed in the following sections for both NO and OH. The third parenthetical term is the number of absorbing molecules in the volume defined by the intersection of the pixel field of view and the laser sheet thickness. The Boltzmann fraction (f_B) expresses the fraction of the total molecular population (N_t) resident in the isolated energy level (or levels) accessed by the laser. For a given level, f_B depends only on fixed spectroscopic parameters and the local gas temperature. The final term is the efficiency with which the fluorescence photons, emitted into all directions, are collected by the imaging optics and focused onto the detector array.

Equation (1) is the basic formula used to reduce the fluorescence data to concentration, mole-fraction, or temperature.

A. NO Fluorescence

The approach for laser-induced NO fluorescence pursued in this program can best be understood by reference to Fig. 4, a partial energy level diagram for NO. The figure shows schematically the grounds $X\,^2\Pi$ electronic state and the first excited electronic state, $A\,^2\Sigma^+$. In the ground electronic state, the first seven vibrational levels are shown. Each vibrational level also contains a manifold of rotational levels which are shown schematically in $v'' = 0$. The vertical arrow at the figure left represents the energy available from a photon near 226 nm (derived from the laser). The laser wavelength is tuned to correspond to the energy of a transition from an isolated rotational level in the ground vibrational level of the lower electronic state, to an isolated rotational level of the lowest vibrational level in the upper electronic state. These rotational transitions are conventionally referred to as (0, 0) band transitions, denoting the vibrational quantum numbers of the upper and lower state, respectively. Molecules elevated to the upper electronic state may transfer to nearby rotational levels or back to the ground electronic state by collisions with neighboring molecules. The rate of transfer back to the ground electronic state is termed quenching (Q). Spontaneous radiative decay competes with the collisional decay through all the allowed transition pathways from the excited state, giving rise to the fluorescence signal. Transitions from the upper electronic state to various vibrational levels in the lower state are denoted by $A_{(0,\,i)}$, where i represents the quantum number of the lower vibrational level.

Transitions on these off-diagonal bands ($\Delta v \neq 0$) shift the fluorescence to longer wavelengths and permit spectral isolation of the weak fluorescence from the laser wavelength. The total collected photon rate is given by

$$A_{\text{eff}} = \sum_i \left[T_{\lambda i} A_{(0,\,i)}\right] \tag{2}$$

where T_λ is the filter transmissivity at wavelength λ. (The wavelength dependence of the intensifier quantum efficiency is essentially constant over the filter transmission curve for both the NO and OH fluorescence detection strategies employed here.) The relative overlap of the filter transmission curve (Acton Research Corporation 254 filter + 2-mm Schott UG-5 filter glass) and the fluorescence spectral bandwidth results in a collected photon rate of only about 5% of the total radiative rate. This penalty in collected signal is due to the requirement for strong rejection of the laser wavelength, important in practical measurements. As we will demonstrate, imaging of the NO fluorescence all the way to the reflective steel tunnel floor was possible without scattering interference from the directly impinging laser sheet.

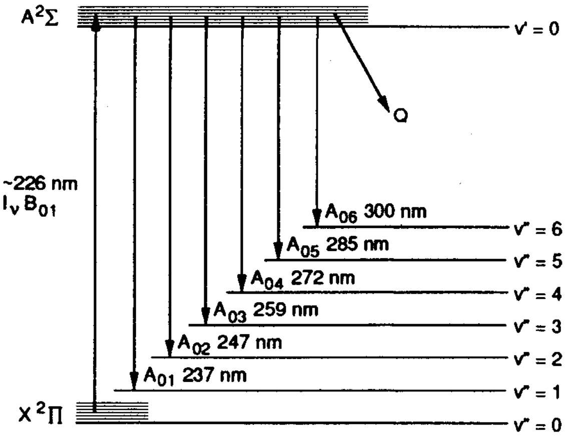

Fig. 4 Schematic energy level diagram showing important processes in laser-induced NO fluorescence.

For this NO excitation/detection strategy, the fluorescence yield may be written as

$$F_y = \frac{A_{\text{eff}}}{A_{v'=0} + Q} \tag{3}$$

Here, $A_{v'=0}$ is the spontaneous radiative decay rate of the laser-excited $v' = 0$ level. In general, the quenching term is written as

$$Q = \sum_i (N_i \sigma_i v_i) \tag{4}$$

where

$N_i \equiv$ number density of collision partner i
$\sigma_i \equiv$ cross section
$v_i \equiv$ mean relative molecular velocity between NO and i.

The sum is over all available quenching partners and the cross sections may vary with the upper state rotational level. For NO in airflows, however, two important simplifications are valid. Firstly, neither the effective radiative transition rate nor the quenching rate is a function of rotational quantum level in NO $A\,^2\Sigma^+$.[9] Hence, the collected photon rate is determined only by the collection filter transmission function, and is not a function of pressure- and temperature-dependent energy transfer rates in the upper manifold. Secondly, for airflows, the sum in Eq. (4) is dominated by the large O_2 cross section, which is independent of temperature over the range of temperatures studied here.[10] Therefore, we may express the quenching term as

$$Q = \text{const} \cdot P \cdot T^{-1/2} \tag{5}$$

where we have gathered together the temperature and pressure dependencies of N_i and v_i. For the nominal 0.3 atm, 1400 K air freestream flows, the total NO quench rate is approximately $7 \times 10^7\ \text{s}^{-1}$ and scales with temperature and pressure according to the above. In combustion or other water vapor-laden flows, the large, temperature dependent cross section of H_2O would have to be included in the calculation of the overall quench rate.[10,11]

The total radiative transfer rate from $v' = 0$ is $5 \times 10^6\ \text{s}^{-1}$, so that for pressures greater than 0.1 atm, $A_{v'=0} << Q$. Hence, the fluorescence yield may be written as

$$F_y = A_{\text{eff}}/Q \sim T^{1/2}/P \tag{6}$$

Using the ideal gas relation, the measured species number density may be expressed as

$$N_t = \chi_i P/RT \tag{7}$$

where $\chi_i \equiv$ the mole-fraction of NO in the airflow. Gathering together the pressure and temperature-dependence of the fluorescence yield and NO number density, we can express the fluorescence equation presented in Eq. (1) as

$$S_F = \text{const} \cdot \chi_i \cdot T^{-1/2} \cdot f_{B(T)} \tag{8}$$

where the constant is a function of laser pulse energy, fixed spectroscopic parameters, and fluorescence collection efficiencies. Variations in the fluorescence signal within an image are only a function of mole-fraction variations (due to chemical reactions) or temperature (with or without chemical reactions). For the convective time from the nozzle throat to the PLIF image planes near the primary injectors, the NO is chemically frozen at superequilibrium levels as the gas expands. Thus, the PLIF image plane contains (in the absence of mixing or burning) a constant mole-fraction of NO with bulk fluid temperature variations due to the Prandtl-Meyer expansion over the rear-facing step, recompression shock from the tunnel floor, and other flow features. Bulk pressure variations will not influence the PLIF signal.

The temperature sensitivity of the fluorescence signal may be tuned by selecting particular ground state rotational levels and exploiting the varying temperature dependence of the Boltzmann population fraction. For example, by choosing a level which increases in population fraction by $\sim T^{1/2}$, the PLIF image will be sensitive only to variations in the mole-fraction of NO. Changes in the mole-fraction reflect the results of chemical reactions in the flowfield. The resultant image will not be sensitive to bulk temperature and pressure variations caused by the compressible flow physics, rather, it will reveal variations due to chemistry. Alternatively, a rotational level may be chosen which accentuates the temperature dependence of the fluorescence signal. For the NO PLIF measurements reported in this article, the NO mole-fraction was essentially constant over most of the image and this latter strategy was selected in order to maximize our sensitivity to the fluid dynamic temperature variations in the image plane.

Temperature, pressure, and flow velocity may also indirectly affect the excitation fluorescence excitation efficiency, the first parenthetical term in Eq. (1). The formally more accurate expression for the excitation efficiency (or rate, with units s^{-1}) is

$$\text{pump rate} = B \int_{\omega} I(\omega) g(\omega)\, d\omega \tag{9}$$

where $g(\omega)$ is the absorption line shape function. In writing Eq. (1), we have assumed that the laser spectral fluence is a "top-hat" profile in frequency, broader than and constant over the entire absorption line shape so that

$$I_{\nu} B = B \int_{\omega} I(\omega) g(\omega)\, d\omega \tag{10}$$

As long as the laser bandwidth substantially exceeds the absorption line shape bandwidth, the assumption of Eq. (10) is a reasonably valid one. As the absorption line shape broadens, this assumption becomes less accurate, although, even for equal bandwidths, the product of the laser line shape and absorption line shapes in the wings of the profiles contributes a small portion to the entire functional product. If the absorption linewidth begins to exceed the laser linewidth, the excitation efficiency and, hence, the fluorescence signal, becomes sensitive to changes in the absorption line shape in the flowfield.

Under most conditions relevant to this study and supersonic combustion in general, the absorption line shapes will be described by a Voigt function, containing contributions from the Doppler (thermal) broadening mechanisms as well as collisional broadening mechanisms. The Doppler width is easily calculated using the formula

$$\Delta\omega_D = 2(2kT \ln 2/mc^2)^{1/2} \omega_A \tag{11}$$

and is a function of temperature alone. The collision width reflects the local collision environment and depends on the composition of the surrounding gas, the overall gas pressure, and temperature. The pressure and temperature dependence is usually separated by expressing the collision width as

$$\Delta\omega_C = \frac{1}{2\pi c} \sum_i \gamma_i P_i \tag{12}$$

where γ_i is the temperature-dependent broadening parameter and P_i is the partial pressure of species i. The sum is over all available collision partners. The total absorption linewidth may be estimated from the formula

$$\Delta\omega_A = (\Delta\omega_C/2) + [(\Delta\omega_C/2)^2 + (\Delta\omega_D)^2]^{1/2} \tag{13}$$

To first order, the temperature and pressure scaling of the collision width is the same as for electronic quenching. Thus, the absorption line shape will expand or contract with temperature and pressure variations in the flowfield. If the laser bandwidth is comparable to or smaller than the absorption bandwidth, the fluorescence signal will also vary with temperature and pressure due to changes in the excitation efficiency expressed in Eq. (10).

Lastly, the absorption line shape may be shifted in frequency by changes in pressure or velocity. The pressure shift is usually expressed as

$$\delta\omega_s = \beta \Delta\omega_C \tag{14}$$

where, for NO, $\beta \simeq -0.303$.[12] The velocity shift is given by

$$\delta\omega_v = (u/c)\omega_A \tag{15}$$

where u is the component of the velocity vector aligned with the laser beam propagation direction.

Table 1 summarizes these linewidths and shifts for the present conditions. In each case, the absorption linewidths and shifts are small compared to the laser linewidth so that the excitation efficiency is not a function of pressure or temperature. In colder, higher pressure flows, however, the absorption linewidth and collisional shifts will be much larger and may be an important factor in interpreting the PLIF images.

B. OH Fluorescence

The strategy developed for OH fluorescence measurements is summarized in Fig. 5. The figure shows schematically the ground $X\,^2\Pi$ ground electronic state and the first excited electronic state, $A\,^2\Sigma^+$. The vertical arrow at the figure left represents the energy available from a photon near 283 nm. The laser wavelength is tuned to correspond to a transition

Table 1 Linewidths and shifts

NO fluorescence	OH fluorescence
$\Delta\omega_L \simeq 0.75\ \text{cm}^{-1}$	$\Delta\omega_L \simeq 0.5\ \text{cm}^{-1}$
$\Delta\omega_C \simeq 0.067\ \text{cm}^{-1}$	$\Delta\omega_C \simeq 0.015\ \text{cm}^{-1}$
$\Delta\omega_D \simeq 0.22\ \text{cm}^{-1}$	$\Delta\omega_D \simeq 0.3\ \text{cm}^{-1}$
$\delta\omega_s \sim 0.02\ \text{cm}^{-1}$	$\delta\omega_s \sim 0.002\ \text{cm}^{-1}$
$\delta\omega_v \sim 0.04\ \text{cm}^{-1}$	$\delta\omega_v \sim 0.1\ \text{cm}^{-1}$
$\Delta\omega_A \simeq 0.27\ \text{cm}^{-1}$	$\Delta\omega_A \simeq 0.31\ \text{cm}^{-1}$

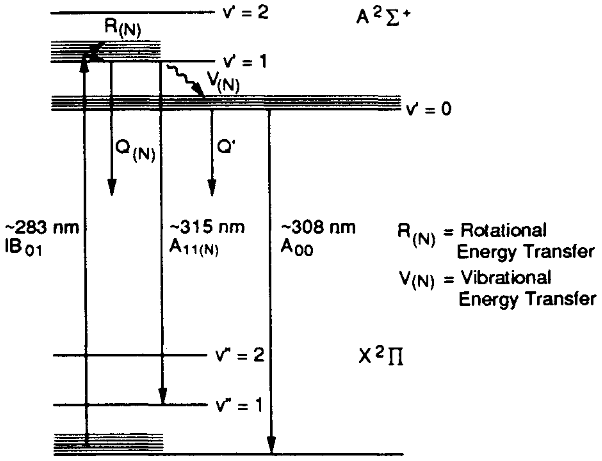

Fig. 5 Schematic energy level diagram showing important processes in laser-induced OH fluorescence.

from an isolated rotational level in the ground vibrational level of the lower electronic state upward to an isolated rotational level of the first excited vibrational level in the upper electronic state. These rotational transitions are conventionally referred to as (1, 0) band transitions, denoting the vibrational quantum numbers of the upper and lower state, respectively. Once in the upper electronic state, various collisional processes transfer population to other rotational levels ($R_{(N)}$) or to the ground vibrational level ($V_{(N)}$) within the upper electronic state. Collisional quenching($Q_{(N)}$ and Q') can remove population completely from both vibrational levels in the upper state. The fluorescence signal is collected from radiative transitions from the (1, 1) band near 315 nm and the collisionally populated (0, 0) band near 308 nm with rates A_{11} and A_{00}. As with the NO fluorescence strategy, the laser excitation wavelength is well-separated from the fluorescence collection band and can be efficiently filtered with combinations of Schott glass (typically 2-mm UG-5 and 1-mm WG-320).

The energy level diagram of Fig. 5 shows the relevant kinetic processes which must be understood in order to calculate the fluorescence yield. They are defined as follows:

$Q_{(N)}$ ≡ quenching rate of laser-excited $v' = 1$ level
$R_{(N)}$ ≡ rate of rotational energy transfer within $v' = 1$
$V_{(N)}$ ≡ rate of vibrational energy transfer from $v' = 1$ to $v' = 0$
Q' ≡ rate of electronic quenching from $v' = 0$
$A_{11(N)}$ ≡ radiative rate for (1, 1) band
A_{00} ≡ radiative rate for (0, 0) band

The (N) subscript indicates that the rate is a function of the initial N-level excited by the laser. Fortunately, the kinetics of the $A\ ^2\Sigma^+$ state in OH in hydrogen and hydrocarbon/air flame environments are reasonably well understood. Crosley and co-workers[13–17] have completed numerous, detailed studies and have determined many relevant kinetic rates. Thus $R_{(N)}$, $V_{(N)}$, $Q_{(N)}$, and $A_{v'v''}$ are known for a variety of conditions.

For our excitation/detection strategy, the fluorescence yield is determined by writing coupled four-level rate equations and assuming steady-state populations. This results in a yield of the following form:

$$F_y = \frac{T_\lambda A_{11(N)} + T_\lambda A_{00} N_0/N_1}{Q_{(N)} + V_{(N)}} \qquad (16)$$

where

T_λ ≡ filter transmission at λ
N_0/N_1 ≡ fractional population in $v' = 0$

The first term in the numerator is the rate of radiative emission from the $v' = 1$ state multiplied by the appropriate filter transmission at the wavelength. The second term is the rate of radiative emission from the $v' = 0$ state multiplied by the filter transmission at this wavelength and multiplied by the fractional population which resides in this level at steady state. The derivation of Eq. (16) assumes that Q and V are both $\gg A$. Since $A_{00} = 1.5 \times 10^6\ \mathrm{s}^{-1}$, $A_{11} = 8.5 \times 10^5\ \mathrm{s}^{-1}$, $Q \sim 5 \times 10^8\ \mathrm{s}^{-1}$ and $V_{(N)} \sim 0.5\ Q$, this assumption is valid for pressure greater than about 0.01 atm.

Our procedure for calculating the OH fluorescence yield has been described in detail in an earlier publication.[18] The principal concern in quantitative interpretation of the OH fluorescence data is the absolute magnitude of the energy transfer terms in Eq. (16) and their potential variation across the image plane due to temperature, composition, and pressure variations. Absolute magnitudes for vibrational energy transfer rates and overall quenching rates are available for a variety of typical flame environments in Refs. 13–17. Of particular importance in the present discussion is the potential variation in the quenching rate due to coupled temperature and composition variations.

The magnitude of these variations in atmospheric pressure flame environments has been examined in detail in several studies. Direct measurements of the fluorescence decay rate in propane-oxygen flames showed that the fluorescence decay rate was constant throughout the flame and scaled linearly with pressure.[19] Large variations in the absolute OH concentration through the measured flame zones confirm that temperature and composition variations existed, but nevertheless, had a negligible impact on the quenching rate. An experimental study comparing saturated and linear fluorescence in atmospheric pressure hydrogen-air diffusion flames resulted in excellent agreement between the saturated (quenching-free) and linear (quenching-dominated) results in all portions of the flame except in fuel-rich zones.[20] In these zones, the assumption of a constant quenching rate resulted in a factor of two underprediction of the OH concentration due to a larger H_2 quenching rate. The authors concluded that in hydrogen-air diffusion flames, as in the present study, the assumption of a quenching rate which is independent of temperature and composition, is valid in all portions of the flow except for fuel rich zones where it may be in error by at most a factor of two.

The impact of quenching variations on OH fluorescence has also been examined by simultaneously measuring the OH fluorescence along with the gas temperature and all major collisional partners.[21] Using the measured collisional partner composition and temperature, the exact quenching rate may be calculated using the species-specific quench rates reported in Refs. 13–18. These authors conclude that, for methane-air flames, the variation in quench rate is limited to about 30% in regions of the flame where significant OH is found. Similar conclusions were reached in Ref. 17. If the local temperature or composition deviate significantly from the nominal flames conditions where peak OH levels are present, the OH concentration falls to levels below typical LIF detection limits. Presumably, the low level of OH at these conditions indicates that OH is not a significant contributor to the local chemistry. Taking these studies together, we conclude that in all regions of the present reacting flow where significant amounts of OH are present, the variation in the quench rate is not a significant barrier to quantitative interpretation of the PLIF images.

From these results one can simplify the temperature and composition dependence of Eq. (4) and write the following equation for the quenching behavior of OH in flame environments:

$$Q = \mathrm{const} \cdot P \qquad (17)$$

In writing Eq. (17), we have retained the pressure dependence of the number density, but collapsed its temperature dependence, along with the temperature and composition dependence of the collision cross section and mean molecular velocity, into the constant. The absolute value of the constant in atmospheric pressure flames is $\sim 6 \times 10^8\ \mathrm{s}^{-1}$, as recommended in Ref. 17. We further assume that the vibrational energy transfer rate in Eq. (16) behaves similarly to the quenching rates. Its magnitude has been measured to be 0.6 of the quench rate.[15] Values of the population ratio, N_0/N_1, have also been measured in flame environments.[15,16] Finally, we calculate A_{11} by assuming that the laser-excited population in $v' = 1$ remains in the directly excited N level. The population in $v' = 0$ following vibrational energy transfer is known to be approximately thermal and independent of the initially excited rotational level in $v' = 1$, therefore, we evaluate A_{00} at $N' = 5$ as an estimate of the average rate of spontaneous radiative decay from $v' = 0$. In this manner, all the terms in Eq. (16) are determined.

The functional form of the fluorescence yield is therefore

$$F_y = [A_{\mathrm{eff}}/(\mathrm{const} \cdot P)] \qquad (18)$$

where the constant is determined according to the procedure described above. We estimate the absolute uncertainty in the fluorescence yield for any given flame environment to be no more than a factor of two. For the well-studied hydrogen-air combustion flames reported here, the uncertainty is less and generally within the typical experimental uncertainties associated with the delivered laser pulse energy, collection efficiency, etc. Combining Eq. (18) with Eq. (1), we can express the temperature, pressure, and number density dependence of the OH fluorescence signal as

$$S_F = \text{const}\cdot f_B \cdot N_{\text{OH}} \cdot P^{-1} \tag{19}$$

In cases where the flowfield is nominally at constant pressure, a useful strategy for quantitative measurements would be to choose the N'' level so that the temperature dependence of the Boltzmann population fraction is minimized over the range of interest. In this limit, the fluorescence signal is only proportional to the OH number density

$$S_F \sim N_{\text{OH}} \tag{20}$$

Since we have assumed constant, or nearly constant, pressure, the variations in number density must be due to chemical reactions rather than bulk fluid dynamics.

Alternatively, in strong pressure-varying flows, a N'' could be chosen so that

$$f_B \sim T \tag{21}$$

$$S_F \sim N_{\text{OH}} \cdot T/P \sim \chi_{\text{OH}} \tag{22}$$

As with the NO excitation strategy developed earlier, variations in the PLIF distribution within an image would be related to chemical reactions alone. For the experiments reported in this article, the OH was confined to the injectant H_2/air interface downstream of the injector bow shock. This portion of the flowfield is nearly constant pressure, so we elected to pursue the first strategy outlined above.

This OH fluorescence strategy is, in principle, subject to the same temperature, pressure, and velocity-dependent linewidth effects discussed in detail in connection with NO fluorescence. The OH line shape under near atmospheric pressure combustion conditions is described, to first order, by a Voigt line shape. In contrast to NO line shapes, however, the OH line shape contains a significantly smaller collisional contribution. Hence, collisional shifting and fluorescence signal diminution due to pressure broadening are not significant at pressures below 5 atm. Table 1 also summarizes the relevant line shapes and shifts for the maximum values encountered in this study. The collisional shift to width ratio is taken from Ref. 22. As with the NO fluorescence, these effects are not significant in the present study.

III. Results

NO PLIF measurements were made in the first PLIF imaging station downstream of the rear-facing step (see Fig. 1). In each case, the field of view (limited by the clear aperture of the laser access window on the top of the tunnel) was 3.8 × 2.9 cm. Two representative PLIF images are presented in Figs. 6 and 7. In these and all PLIF images in this article, the bottom of the image corresponds to the bottom of the flow tunnel and the images are obtained with a single laser pulse. The signal levels are mapped according to the gray scale shown, corresponding to a linear mapping of the 256 digital signal levels. In Fig. 6, the flowfield consists of the simple expansion over the step with no injection, as described in Fig. 2. In this series of experiments, the laser was tuned to the Q_{22} + $R_{12}(7)$ transition at 226.72 nm. The N'' = 7 level has a negative temperature dependence over the range in the flow so that the temperature sensitivity of the PLIF image is enhanced. The left side of the image is defined by the upstream edge of the laser sheet which does not correspond to the edge of the imaged region. In initial testing, the tunnel apparently moved a few millimeters during firing and it was not possible to exactly position the fixed camera with respect to the tunnel.

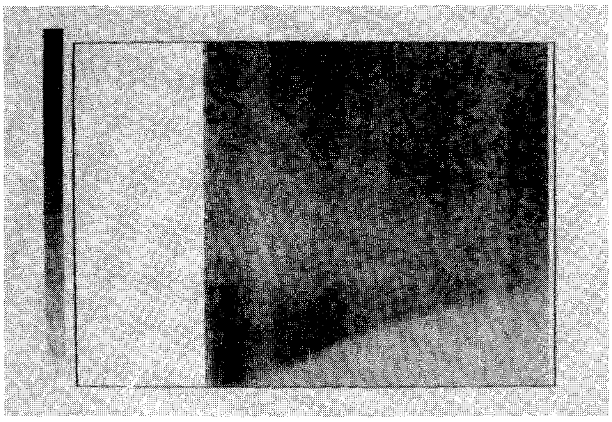

Fig. 6 NO PLIF distribution without injection. The gray scale intensities correspond to a temperature range from 600 K (dark) to 1800 K (light).

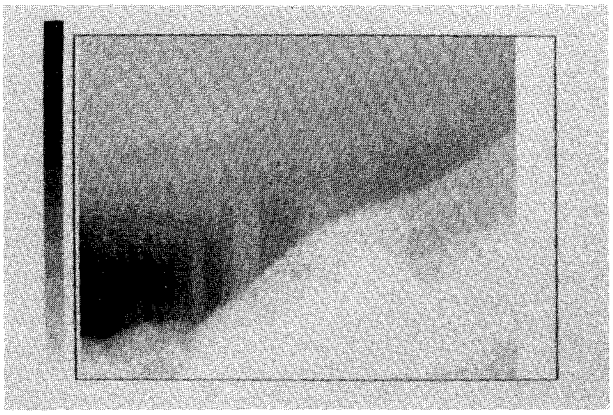

Fig. 7 NO PLIF distribution with injection. The gray scale temperature range is the same as in Fig. 6.

The absolute signal levels in the freestream (at the upper left corner of the image) correspond to the nominal flow condition of 1500 K, 0.3 atm, and ~1 × 10^{17} cm^{-3}. The fully expanded flow is in the lower left corner of the image and the signal levels there are approximately 1.5 times greater. The recompression shock is clearly visible, initially straight, then curving slightly through the nonuniform flow region. The signal level across the recompression shock is about 33% of the level in the fully expanded flow due to the higher temperature there, and about 60% of the signal level in the freestream. The light band across the center of the image was a persistent feature in each of the images acquired during this first series of PLIF experiments and was not expected from our flowfield predictions. It was subsequently determined that this band was due to a cloud of particulate remaining from the shock-tube driver fabrication which was lifted as a jet along the tunnel floor during early flow times. The fluorescence signal is diminished where the particulate jet is present due to extinction of the fluorescence as it propagates across the flow toward the imaging detector. Cleaning of the tunnel and a change in operational procedures removed this effect and subsequent data are free from this interference.

Figure 7 is an image of the same plane in the flow, now with helium injection. In this image, the R_{11} + $Q_{21}(13)$ transition was excited, providing slightly higher signal levels while preserving the temperature sensitivity. This image is free from particulate interference and the contours of the Prandtl-Meyer expansion fan, made visible by the decreasing temperature, are clearly visible. The fan lines terminate beyond the left side of the image at the downstream edge of the step. The highest signal levels, again, occur in the fully expanded flow at the lower left portion of the image. The signal ratio from the freestream to the fully expanded flow is consistent with a temperature variation from ~1320 to ~550 K. A portion of the raw fluorescence image near the center of the image was saturated during the experiment. This was due to the relatively higher laser energy in the central part of the sheet. During the correction procedure for the laser energy variation these data were naturally corrupted since their actual signal levels were beyond the maximum level of the A/D converter. The vertical stripes at this location reflect the small variations in laser sheet intensity imposed upon the artificially constant signal data and should be ignored. This nonideal image performance is a typical consequence of the single-shot nature of the shock tunnel experiments, where on-line adjustment of detector gain is not possible.

The injection substantially modifies the remainder of the downstream flowfield. Rather than a recompression shock, the injectant gas sets up a strong bow shock in the flow. The fluorescence signal across the bow shock immediately decreases due to the higher temperature there. Along the flow streamlines, it decreases further, eventually disappearing, as the NO mixes with the helium injectant. Downstream of the bow shock, the NO is no longer a constant mole-fraction constituent of the gas and the PLIF image reflects the combined effects of temperature variations and mixing. In this region the PLIF image is a qualitative visualization of the injectant mixing. Interestingly, the lower left corner of the image reveals a sharp boundary between the expanded flow (high signal levels) and the entrainment of the injectant gas into the recirculation zone (low signal levels).

The variation in the NO PLIF fluorescence is consistent with the expected inviscid flow temperature variations, but the existing data base is too small to justify strong claims regarding the ultimate accuracy of our approach. In the experiments without injection, the signal levels in the fully expanded region and the recompression region are somewhat lower with respect to the freestream flow than expected. This is at least in part explained by the laser sheet extinction in the particulate jet. In the single experiment with injection, the fully expanded temperature, as measured by the PLIF data, is about 550 K, whereas the expected inviscid flow temperature is approximately 750 K. In the absence of a detailed flow model, it is not presently clear whether this discrepancy is due to a measurement error or to a more complex flow phenomenon not contained in our simple model. The overall trends of the data, however, are correct and the PLIF image clearly reveals structure of the flow that could not otherwise be observed and strongly demonstrate the potential for quantitative PLIF measurements in high temperature, high pressure, supersonic flows.

The first OH PLIF experiments were conducted in the same flow plane as the NO PLIF experiment shown in Figs. 6 and 7. Approximately 2 mJ of laser energy was delivered in the 3-cm sheet. An example image is shown in Fig. 8. The field of view for all of the OH images was 3 × 2.25 cm. The peak fluorescence intensities in this image correspond to approximately 50 photons per pixel incident on the intensifier photocathode. Using the spectroscopic parameters developed above, and assuming a nominal flow pressure of 0.5 atm and a temperature of 2500 K, this corresponds to a peak OH concentration of $\sim 10^{15}$ cm^{-3}, or about 600 ppm. In this near-field region of the jet, the OH is confined to the mixing layer between the injectant hydrogen and the hot air behind the bow shock. A low-level "cloud" of OH surrounds the bright central filament and appears to extend upstream to the shock boundary. Ignition takes place rapidly and the existence of large scale mixing features (on the order of the jet diameter) can be seen in the shear layer, even at these relatively high Mach numbers. A low level of OH is visible in the recirculation zone upstream of the nozzle as well. Finally, a low level of OH is visible underneath the jet in the lower right side of the image due to entrainment of air by axial vorticity in the flow.

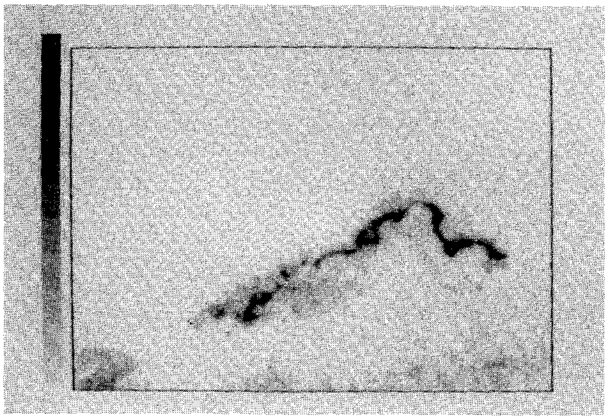

Fig. 8 Instantaneous OH distribution above first H_2 injector.

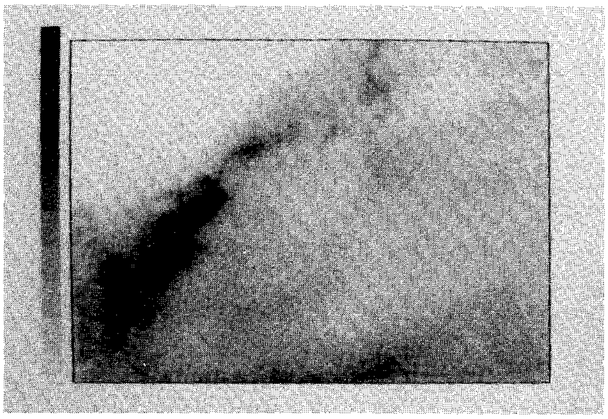

Fig. 9 OH PLIF image above second injector.

In the next experiment, the excitation laser sheet and camera were moved downstream to image the OH distribution in the vicinity of the second injector station. Figure 9 shows PLIF images taken with the same magnification as Fig. 8. The OH-laden plume from the first injector impinges on the second injector plume near the right side of the image. The second injector is angled at 60 deg to the flow, whereas the first is at 30 deg. Thus, the plume from the second injector penetrates into the freestream flow more quickly. A similar filament of high OH levels is evident, marking the boundary between the injectant gas and the hot air. A puzzling feature in Fig. 9 is the apparently high levels of OH on the tunnel floor. While some trapping of OH in the hot tunnel boundary layer (where the flow stagnates) is expected, it is not physically reasonable that high OH concentrations exist directly over the injector along the central plane sliced by the laser sheet. We believe the signal level in this portion of the image is due to out of plane chemiluminescent or thermal emission from the spreading plume which is integrated by the detector during the ~1 μs gate of the intensifier.

Attempts to image the OH distribution at the next window station (23 step heights downstream) were obscured by strong thermal emission from the hot product gases across the 7.5-cm tunnel. We are currently developing a fast-gating imaging system with gate times on the order of 10 ns. This will reduce the observed emission interference below our detection limit. The fluorescence signal will be reduced by approximately a factor of 2 due to the reduced quantum efficiency of the fast-gating intensifier tube. Further improvement in the fluorescence to emission ratio can be obtained using a Nd:YAG laser system instead of an excimer laser system, since the Nd:YAG-based system has about an order of magnitude higher pulse energy at the OH excitation wavelength.

IV. Conclusions

This article has described details of a successful series of experiments demonstrating applications of PLIF measurements of OH and NO in model scramjet combustor test facilities. Issues associated with quantitative interpretation of PLIF measurements in compressible reacting flows were discussed in detail, and strategies were developed for measurements of species number density, volume (or mole) fraction, and static gas temperature. Potential interferences from hot gas luminescence were identified and solutions offered. The application of PLIF to pulsed flow facilities used for supersonic combustion research was shown to produce meaningful data on the temperature variations in nonreacting portions of the flow and on the qualitative structure of the reaction zone in combusting flows. Limitations to the quantitative interpretation of the fluorescence data in these flows were discussed in detail. Future work in our laboratory will extend the measurement base in this facility to include velocity field measurements and combustion product species measurements.

Acknowledgment

This work was support by the Air Force Wright Laboratory under a Phase II SBIR Contract F33615-88-C-2907, John Smith, Contract Monitor.

References

[1] McMillin, B. K., Lee, M. P., and Hanson, R. K., "Planar Laser-Induced Fluorescence Imaging of Shock Tube Flows with Vibrational Nonequilibrium," *AIAA Journal*, Vol. 30, No. 2, 1992, p. 436.

[2] Cassady, P. E., and Lieberg, S. F., "Planar Laser-Induced Fluorescence Measurements in Hypersonic Air Flowfields," AIAA 22nd Fluid Dynamics, Plasma Dynamics, and Lasers Conf., AIAA Paper 91-1492, June 1991.

[3] Lee, M. P., McMillin, B. K., Palmer, J. L., and Hanson, R. K., "Planar Fluorescence Imaging of a Transverse Jet in a Supersonic Cross Flow," *Journal of Propulsion and Power*, Vol. 8, No. 4, 1992, p. 729.

[4] Hartfield, R. J., Hollo, S. D., and McDaniel, J. C., "Experimental Investigation of a Supersonic Swept Ramp Injector Using Laser-Induced Iodine Fluorescence," AIAA 21st Fluid Dynamics, Plasma Dynamics and Lasers Conf., AIAA Paper 90-1518, June 1990.

[5] Roshko, A., and Thonke, G. T., "Observations of Turbulent Reattachment Behind an Axisymmetric Downstream-Facing Step in Supersonic Flow," *AIAA Journal*, Vol. 4, No. 6, 1966, p. 975.

[6] Stein, A., "Supersonic Flow Separation on a Backward Facing Step," Rept. AS-66-18, AFOSR Grant 268-66, 1966.

[7] Sirleix, M., Mirande, J., and Deleny, T., "Basic Experiments on the Reattachment of a Supersonic Stream," RAE, Library Translation 1196, 1965.

[8] Hortzaiker, J. R., "An Experimental Investigation of the Affect of the Approaching Boundary Layer on the Separated Flow Behind a Downstream Facing Step," National Aerospace Laboratory, NLR TR 700334, The Netherlands.

[9] McDermid, I. S., and Laudenslager, J. B., "Radiative Lifetimes and Electronic Quenching Rate Constants for Single-Photon-Excited Rotational Levels of NO ($A\ ^2\Sigma^+$, $v' = 0$)," *Journal of Quantitative Spectroscopy Radiative Transfer*, Vol. 27, No. 5, 1982, p. 483.

[10] Raiche, G. A., and Crosley, D. A., "Temperature Dependent Quenching of the $A\ ^2\Sigma^+$ and $B\ ^2\Pi$ States of NO," *Journal of Chemical Physics*, Vol. 92, No. 9, 1990, p. 5211.

[11] Cattolica, R. J., Mataga, T. G., and Cavolowsky, J. A., "Electronic Quenching and Vibrational Relaxation of NO $A\ ^2\Sigma^+$ ($v' = 1$, $v' = 0$) by Collisions with H_2O," *Journal of Quantitative Spectroscopy & Radiative Transfer*, Vol. 42, No. 6, 1989, p. 499.

[12] Allen, M. G., and Davis, S. J., "Velocity Measurements in High Temperature Gases Using Laser-Induced NO Fluorescence," Final Rept. for USAF Systems Division Contract F33615-90-C-209, Andover, MA, 1991.

[13] Smith, G. P., and Crosley, D. R., "Quantitative Laser-Induced Fluorescence in OH: Transition Probabilities and the Influence of Energy Transfer," *18th Symposium (Int.) on Combustion*, Combustion Inst., Pittsburgh, PA, 1981, p. 1511.

[14] Crosley, D. R., and Smith, G. P., "Rotational Energy Transfer and LIF Temperature Measurements," *Combustion and Flame*, Vol. 44, No. 27, 1982, p. 27.

[15] Smith, G. P., and Crosley, D. R., "Vibrational Energy Transfer in $A\ ^2\Sigma^+$ in OH in Flames," *Applied Optics*, Vol. 22, No. 10, 1983, p. 1428.

[16] Copeland, R. A., Wise, M. L., and Crosley, D. R., "Vibrational Energy Transfer and Quenching of OH ($A\ ^2\Sigma^+$, $v' = 1$)," *Journal of Physical Chemistry*, Vol. 92, 1988, p. 5710.

[17] Garland, N. L., and Crosley, D. R., "On the Collisional Quenching of Electronically Excited OH, NH, and CH in Flames," *21st Symposium (Int.) on Combustion*, Combustion Inst., Pittsburgh, PA, 1986, p. 1693.

[18] Allen, M., Davis, S., and Donohue, K., "Planar Measurements of Instantaneous Species and Temperature Distribution in Reacting Flows: A Novel Approach to Ground Testing Instrumentation," AIAA/SAE/ASME/ASEE 26th Joint Propulsion Conf., AIAA Paper 90-2383, July 1990.

[19] Stepowski, D., and Cottereau, M. J., "Study of the Collisional Lifetime of Hydroxyl ($^2\Sigma^+$, $v' = 0$) Radicals in Flames by Time-Resolved Laser-Induced Fluorescence," *Combustion and Flame*, Vol. 40, 1981, p. 65.

[20] Drake, M. C., and Pitz, R. W., "Comparison of Turbulent Diffusion Flame Measurements of OH by Planar Fluorescence and Saturated Fluorescence," *Exp. in Fluids*, Vol. 3, 1985, p. 283.

[21] Barlow, R. S., and Collignon, A., "Linear LIF Measurements of OH in Nonpremixed Methane-Air Flames: When are Quenching Corrections Unnecessary," AIAA 29th Aerospace Sciences Meeting, AIAA Paper 91-0179, Jan. 1991.

[22] Shirinzadeh, B., Bakalyar, D. M., and Wang, C. C., "Measurement of Collision-Induced Shift and Broadening of the Ultraviolet Transitions of OH," *Journal of Chemical Physics*, Vol. 82, 1985, p. 2877.